Check for updates

Epitaxial van der Waals contacts of 2D TaSe$_2$-WSe$_2$ metal–semiconductor heterostructures†

Peiyu Qiao,[a,b] Jing Xia,*[a,b] Xuanze Li,[a,b] Yuye Li,[a,b] Jianyu Cao,[a,b] zhongshi zhang,[a,b] Heng Lu,[a,b] Qing Meng,[b,c] Jiangtao Li[b,c] and Xiang-Min Meng (ID) *[a,b]

The electronic contact between two-dimensional (2D) transition metal dichalcogenide (TMD) semiconductors and metal electrodes is a formidable challenge due to the undesired Schottky barrier, which severely limits the electrical performance of TMD devices and impedes the exploration of their unconventional physical properties and potential electronic applications. In this study, we report a two-step chemical vapor deposition (CVD) growth of 2D TaSe$_2$-WSe$_2$ metal–semiconductor heterostructures. Raman mapping confirms the precise spatial modulation of the as-grown 2D TaSe$_2$-WSe$_2$ heterostructures. Transmission electron microscopy (TEM) characterization reveals that this two-step method provides a high-quality and clean interface of the 2D TaSe$_2$-WSe$_2$ heterostructures. Meanwhile, the upper 1T-TaSe$_2$ is formed heteroepitaxially on/around the pre-synthesized 2H-WSe$_2$ monolayers, exhibiting an epitaxial relationship of $(20-20)_{TaSe_2}//(20-20)_{WSe_2}$ and $[0001]_{TaSe_2}//[0001]_{WSe_2}$. Furthermore, characterization studies using a Kelvin probe force microscope (KPFM) and electrical transport measurements present compelling evidence that the 2D metal–semiconductor heterostructures under investigation can improve the performance of electrical devices. These results bear substantial significance in augmenting the properties of field-effect transistors (FETs), leading to notable improvements in FET mobility and on/off ratio. Our study not only broadens the horizons of direct growth of high-quality 2D metal–semiconductor heterostructures but also sheds light on potential applications in future high-performance integrated circuits.

Introduction

Following the guidance of Moore's law,[1] traditional silicon-based transistors have continued to shrink. However, when the channel of the silicon transistor is reduced to less than 5 nm, the silicon-based semiconductor has approached its physical limit, and short channel effects (SCEs) will severely inhibit the performance of the device.[2] It is critical to create novel channel materials to replace traditional silicon-based semiconductors. In recent years, two-dimensional (2D) transition metal dichalcogenides (TMDs)[3–9] have attracted significant

[a]Key Laboratory of Photochemical Conversion and Optoelectronic Materials, Technical Institute of Physics and Chemistry, Chinese Academy of Sciences, Beijing, 100190, P. R. China. E-mail: mengxiangmin@mail.ipc.ac.cn, xiajing@mail.ipc.ac.cn
[b]Centre of Material Science and Optoelectronic Engineering, University of Chinese Academy of Science, Beijing, 10049, P. R. China
[c]Key Laboratory of Cryogenics, Technical Institute of Physics and Chemistry, Chinese Academy of Sciences, Beijing 100190, P. R. China
†Electronic supplementary information (ESI) available: Further details of the experimental design. OM, SEM, Raman, and AFM characterization of WSe$_2$ and TaSe$_2$. HAADF-STEM analysis of cross-sectional samples of 2D multilayer TaSe$_2$ and multilayer WSe$_2$ heterostructures. Schematic diagram of FET device preparation. See DOI: https://doi.org/10.1039/d3nr03538g

attention because of their diverse conductivity characteristics, behaving as insulators,[10,11] semiconductors,[12–14] and metals.[4,15–18] Additionally, in contrast to three-dimensional (3D) silicon-based semiconductors, 2D TMDs possess atomic-scale thickness and inherent intralayer bonding properties without surface dangling bonds, which gives 2D TMDs excellent immunity to short-channel effects.[19] In the past few years, there has been a surge of interest in 2D field-effect transistors (FETs), with several research groups reporting significant progress in this field. Notably, Desai et al.[20] developed 1D2D-FETs utilizing 1 nm diameter carbon nanotubes as gate electrodes and MoS$_2$ as the channel material. Wu et al.[21] successfully synthesized side-wall transistors with a gate length of only 0.34 nm, demonstrating excellent switching characteristics with an impressive on/off ratio of up to 1.02×10^5. These advancements in 2D FET technology represent a significant step forward in the development of next-generation semiconductor devices, with the potential to achieve unprecedented levels of performance and functionality. As such, continued research in this area promises to yield exciting breakthroughs in the near future.

However, the primary challenge faced by 2D FETs is the significant contact resistance[22–24] that occurs at the interface

between the 2D semiconductor and metal electrodes. This resistance substantially impacts the performance of 2D electronic devices. The fundamental cause of this resistance is the formation of a Schottky barrier between the metal electrode and the semiconductor. In the case of 2D semiconductor materials, several factors contribute to the formation of Schottky barriers. Firstly, the energy difference between the work function of the metal and the electron affinity of the 2D semiconductor and the type of 2D semiconductor determines the type of contact between the metal electrode and the 2D semiconductor.[25] Secondly, 2D materials possess an abundance of surface states due to their ultrathin thickness, which can lead to Fermi-level pinning,[26] along with metal-induced gap states,[27] resulting in the formation of Schottky barriers. Thirdly, the conventional lithography process leaves behind polymeric residues,[28] while typical thermal evaporation processes usually involve atom or cluster bombardment and strong local heating at the contact region, which could damage the crystal lattice at or near the interface, contributing to the formation of Schottky barriers.[29] As a result, there is a pressing need to synthesize high-quality contact between metal and 2D semiconductors. Achieving this goal would help address the significant contact resistance challenge and improve the performance of 2D electronic devices.

Thus, to address the challenges of the metal–2D semiconductor contact, various strategies have been proposed to optimize the interface between metal electrodes and 2D semiconductors. These strategies include manufacturing clean edge contact to 2D semiconductors,[30,31] phase engineering of 2D semiconductors to construct planar metal–semiconductor heterostructures,[32,33] formation of clean interfaces *via* van der Waals (vdWs) contacts using graphene,[34] mechanical transfer of metal films,[35] using hexagonal boron nitride (h-BN) as the tunnel barrier,[10] and synthesis of metal–semiconductor heterostructures by vapour phase epitaxy.[36–42] Among these strategies, vapour phase epitaxy technology is an effective method to create vdWs heterostructures with a low contact barrier at the clean vdWs interface. For instance, Zhang *et al.*[38] demonstrated a controllable epitaxial growth of NbS_2-WS_2 lateral heterostructures *via* a facile "two-step" chemical vapor deposition (CVD) route. The electrical transport measurements showed explicit Schottky junction features with well-defined rectification, indicating potential application in electronic devices. Additionally, Yu *et al.*[41] developed a one-step CVD method for the synthesis of $NbSe_2$/Nb-doped-WSe_2 metal/doped-semiconductor vdWs heterostructures with doping-controlled Ohmic contacts. The contact resistance RC value using the $NbSe_2$ contact was 2.46 kΩ μm, which is approximately 29 times lower than that using a metal contact. These results indicate that it is feasible in practice to achieve high-quality electrical contacts of 2D vdWs crystals as various vertical metal–semiconductor stacks, which can promote the development of next-generation electronics, optoelectronic devices, and energy-related fields.

In this work, we demonstrate the two-step CVD synthesis of $TaSe_2$–WSe_2 heterostructures. The crystal structure, chemical composition, and epitaxial relationship between the 2H-WSe_2 and 1T-$TaSe_2$ layers have been investigated using atomic force microscopy (AFM), Raman spectroscopy, and transmission electron microscopy (TEM). The Kelvin probe force microscope (KPFM) characterization reveals a contact potential height of ∼680 mV between 2H-WSe_2 and 1T-$TaSe_2$ layers. Furthermore, the tests of back-gated FETs demonstrate the enhancement of the electronic contact at the heterointerface. The findings of our work demonstrate the feasibility of using CVD synthesis to create heterostructures with precise control of layer thickness and composition. These results have significant implications for the design and optimization of 2D electronic devices and may facilitate the development of advanced technologies for future applications.

Experimental

CVD of monolayer WSe_2

Monolayer WSe_2 films were synthesized *via* an ambient pressure CVD method, utilizing tungsten trioxide (WO_3) powder and selenium (Se) as precursors. The CVD process involved placing a ceramic boat containing WO_3 powder (50 mg, 99%, Alfa) in the center of a tubular furnace, while Se powder (300 mg, 99.5%, Alfa) was placed in a homemade quartz boat and positioned approximately 10 cm upstream from the furnace center. A sapphire substrate was employed as the growth substrate and placed downstream at 3 cm from the heating center. Before the growth, the tubular furnace was purged using 400 sccm Ar gas for 10 minutes. Once the furnace center zone was heated to 950 °C within 50 minutes, it was maintained at this temperature for 30 minutes before naturally cooling down to room temperature. Upon reaching 950 °C, the Ar gas was switched to a mixed Ar/H_2 flow (76 sccm/4 sccm), as depicted in Fig. S1a.†

CVD of 2D $TaSe_2$-WSe_2 heterostructures

A different furnace was employed for the epitaxial growth of 1T-$TaSe_2$. The sapphire substrate containing the WSe_2 layers was placed in the center of the heating zone and heated to 850 °C. Commercial $TaCl_5$ (20 mg, 98%, Alfa) and Se (200 mg) were utilized as precursors and heated to 400 and 300 °C, respectively. Prior to furnace heating, a mixed Ar/H_2 flow (380 sccm/20 sccm) was introduced for 20 minutes to flush the gas path and establish a stable chemical reaction environment. The furnace was then heated to 850 °C within 45 minutes and maintained at this temperature for 10 minutes and then allowed to naturally cool down to room temperature. Upon reaching 850 °C, the flow rate was adjusted to 76 sccm/4 sccm, as depicted in Fig. S1b.†

Transfer of samples

To prepare the as-grown heterostructures for analysis, a thin film of poly(methyl methacrylate) solution (PMMA, 4 wt%, 950 K molecular weight) was initially spin-coated onto the samples at 1000 rpm for 1 minute. The samples were then

heated on a hot plate at 110 °C for 10 minutes, after which 1 mm wide PMMA strips were removed using a blade at the substrate edges. The substrate with the sample upside down was then immersed in deionized water for 2 hours to extract the PMMA/heterostructure films from the sapphire substrates. Next, a holey carbon film supported on copper grids or a pre-etched conductive silicon substrate (using HF) was utilized to extract the PMMA/heterostructure film, which was then dried in an oven at 60 °C for 2 hours to remove any remaining water and enhance adhesion between the PMMA/heterostructure film and the substrate (copper grid or silicon). Finally, the PMMA layer was removed by immersion in dichloromethane for 30 minutes.

Materials characterization

Optical images were obtained using a Nikon Eclipse Ti-U inverted microscope fitted with a Nikon Digital Sight CCD. SEM images were collected using a Hitachi S-4800 field-emission microscope operating at 15 kV. Raman spectra and mappings were performed with the Renishaw inVia Raman microscope and Nanophoton Raman 11 microscope. Bruker Dimension FastScan was used for AFM and KPFM characterization. KPFM characterization was carried out using a doped silicon tip (PFQNE-AL, Bruker) with a probe radius of approximately 5 nm and a spring constant of around 0.8 N m^{-1} under peak force mode, with a 60 nm lift scan height. TEM and STEM images, and EDS maps were acquired using an aberration-corrected JEM-ARM300F microscope operating at 300 kV, located at the Technical Institute of Physics and Chemistry, Chinese Academy of Sciences, Beijing. Cross-sectional samples for TEM were fabricated using an FEI Helios-600i focused ion beam (FIB).

Device fabrication and characterization

The 2D material grown on the sapphire substrate was initially transferred to (n++) 300 nm-SiO$_2$/Si substrates using the PMMA method. Subsequently, TaSe$_2$–WSe$_2$ heterostructure bands were generated by etching the TaSe$_2$–WSe$_2$ heterostructure with a focused helium ion beam in a helium ion microscope (HIM) system. Standard electron-beam lithography (EBL) and a lift-off process with acetone were used to fabricate the source/drain electrodes. Following fabrication, the devices were annealed at 250 °C for 2 hours under an Ar atmosphere to enhance the electronic contact. The electrical properties of the devices were measured in an atmospheric environment using a Lakeshore probe station and a Keithley-4200 SCS semiconductor parameter analyzer.

Results and discussion

Herein, we have successfully achieved a controlled epitaxial growth of 2D TaSe$_2$-WSe$_2$ heterostructures using a two-step CVD method as shown in Fig. 1a. Large-area 2H-WSe$_2$ monolayers were first synthesized by selenization of WO$_3$ on sapphire substrates (Fig. S1a†) at 950 °C, which were identified using optical microscopy (OM), Raman spectroscopy, and atomic force microscopy (AFM) (Fig. 1b and Fig. S2†). Subsequently, the growth of multilayer 1T-TaSe$_2$ on the pre-obtained 2H-WSe$_2$ monolayers was performed by selenylation of TaCl$_5$ at 850 °C (Fig. S1b†). SEM images (Fig. S3†) and schematic diagrams (Fig. S4†) further provide more details about the growth process. The prepared 2D WSe$_2$ and 2D TaSe$_2$-WSe$_2$ heterostructures exhibit mainly triangular shapes with a side length of several microns, as shown in optical images (Fig. 1b and c). The sharp optical contrast between the border (bright contrast) and the central region (dark contrast) can also be distinguished, marking the successful epitaxial growth of a new layer on the bottom WSe$_2$. This can be further confirmed by scanning electron microscopy (SEM) images (Fig. 1d). Furthermore, Fig. 1e gives a representative AFM image of the as-grown 2D TaSe$_2$-WSe$_2$ heterostructure. The apparent colour contrast in the AFM image indicates that the heterostructure possesses a smooth central surface and a raised edge structure and the thickness of the edges is found to be ~15 nm. By varying the growth parameters, the thickness of TaSe$_2$ on the heterojunction can be as thin as several nanometres or even a single layer, as shown in Fig. S5.† Notably, we also successfully obtained a few-layers thick TaSe$_2$ deposit on sapphire substrates using the same method, which was characterized by OM, Raman spectroscopy, and AFM (Fig. S6†).

Raman spectroscopy was further conducted to study the spatial modulation of the structural and optical characteristics of the 2D TaSe$_2$-WSe$_2$ heterostructures using a 532 nm laser. As shown in Fig. 1f, a typical optical image of a triangular sample used for Raman characterization is displayed. Raman spectra were collected from different areas of the sample to observe the spatial modulation of the heterostructure. As illustrated in Fig. 1g, the Raman spectra obtained from the central region (k in Fig. 1f) exhibit two characteristic peaks at 249 cm^{-1} and 259 cm^{-1}, corresponding to the E$^1_{2g}$, and A$_{1g}$ Raman modes of 2H-WSe$_2$,[43] respectively. On the other hand, the Raman spectra collected from the edge area (j and l in Fig. 1f) display five characteristic Raman peaks located at 138 cm^{-1}, 209 cm^{-1}, 234 cm^{-1}, 249 cm^{-1}, and 259 cm^{-1}. Among these, the peaks at 138 cm^{-1}, 209 cm^{-1}, and 234 cm^{-1} are attributed to the E$_{1g}$, E$_{2g}$, and A$_{1g}$ Raman modes of 1T-TaSe$_2$,[44] respectively, while the remaining two peaks are related to the Raman modes of 2H-WSe$_2$. Interestingly, the Raman spectra acquired from the edge area exhibited Raman peaks of both TaSe$_2$ and WSe$_2$, indicating the coexistence of the two different materials. To visualize the spatial distribution of TaSe$_2$ and WSe$_2$ in the heterostructure, Raman intensity maps of 209 cm^{-1} (E$_{2g}$ mode for TaSe$_2$) and 249 cm^{-1} (E$^1_{2g}$ mode for WSe$_2$) are generated and shown in Fig. 1h and i, respectively. The Raman intensity map of TaSe$_2$ (Fig. 1h) reveals that the edge area is composed of TaSe$_2$. In the Raman intensity maps of WSe$_2$ (Fig. 1i), the brighter contrast of the central region compared to the edge area is attributed to the fact that most of the Raman signal is shielded by the upper layer of TaSe$_2$. In general, our findings demonstrate the spatial modulation of the structural and optical characteristics of the 2D TaSe$_2$-WSe$_2$ heterostructures.

Fig. 1 (a) Fabrication strategy for 2D $TaSe_2$-WSe_2 heterostructures on the sapphire substrate. Optical images of (b) the large-area monolayer WSe_2 and (c) the large-area 2D $TaSe_2$-WSe_2 heterostructure. (d) SEM image of 2D $TaSe_2$-WSe_2 heterostructures with triangular shapes. (e) AFM image and height profiles of the 2D $TaSe_2$-WSe_2 heterostructure. (f) Optical image of a representative 2D $TaSe_2$-WSe_2 heterojunction. (g) Raman spectra collected from the regions marked j–l in (f), respectively. (h) and (i) Raman intensity maps of Raman modes at 209 cm^{-1} ($TaSe_2$) and 249 cm^{-1} (WSe_2), respectively.

The elemental composition and crystal structure of the 2D $TaSe_2$-WSe_2 heterojunction were first characterized by aberration-corrected scanning transmission electron microscopy (STEM) and energy dispersive X-ray spectroscopy (EDS). A low-magnification high-angle annular dark-field aberration-corrected scanning transmission electron microscopy (HAADF-STEM) image (Fig. 2a) of the 2D $TaSe_2$-WSe_2 heterojunction displays a triangular morphology with distinct contrast between the marginal and central regions, indicating a significant difference in thickness between the stacked $TaSe_2$ and the underlying WSe_2 layers. EDS maps (Fig. 2b–d) of the red dashed area shown in Fig. 2a reveal that the W element has a uniform intensity distribution, while Ta is present only in the edge area. These findings suggest that the edge portion of the flake sample consists of stacked $TaSe_2$ and the bottom layer is WSe_2. Additionally, this analysis is confirmed by selected area electron diffraction (SAED) patterns (Fig. 2e–g) of three different regions (shown in Fig. 2a) labeled with purple (e), yellow (f), and white (g) dots. It is observed that Fig. 2f reveals only one set of six-fold symmetrical diffraction spots, which matched with that of hexagonal WSe_2. Due to the lattice constant of 1T-$TaSe_2$ (a = ~0.345 nm) being slightly larger (mismatch only ~4.6%) than that of 2H-WSe_2 (a = ~0.329 nm), it is difficult to differentiate the SAED patterns (Fig. 2e and g) of the stacked regions (dots e and g) from those of low-order reflections. However, in the high-order reflections, the spots

separate, which allows a chance for identification, as illustrated in Fig. 2h. The enlarged SAED pattern displays two sets of well-aligned six-fold diffraction spots. The inner set (red dotted line) originates from the $TaSe_2$, while the outer set (yellow dotted line) belongs to WSe_2. The good alignment of the two sets of spots offers clear and convincing evidence that $TaSe_2$ is grown epitaxially on the underlying WSe_2 layer, and the epitaxial relationship between them can be described by $(20-20)_{TaSe_2}//(20-20)_{WSe_2}$ and $[0001]_{TaSe_2}//[0001]_{WSe_2}$.

To further determine the stacking structure of $TaSe_2$ and WSe_2, a high-magnification HAADF-STEM image of the 2D $TaSe_2$-WSe_2 heterostructure interface was collected and is shown in Fig. 2i. Careful inspection of the interface reveals a clear layer-by-layer stacking interface and well-aligned orientation, thus indicating the vdWs epitaxial growth feature in the vertical stacks. The lattice fringes of the (10−10) plane of $TaSe_2$ and WSe_2 are found to be approximately 0.3 nm and 0.28 nm, respectively, which are consistent with the interplanar spacings of 1T-$TaSe_2$ and 2H-WSe_2. Furthermore, atomic-resolution HAADF-STEM images of different regions show clear 2H-phase WSe_2 and 1T-phase $TaSe_2$ structures, demonstrating the high crystal quality of the heterostructure (Fig. 2j and k). These findings indicate that the two-step CVD method used has not destroyed the underlying WSe_2 or produced an alloying phase. Typically, cross-sectional HAADF-STEM images (Fig. 2l and m) show that the upper 1T-$TaSe_2$ is coherently stacked on mono-
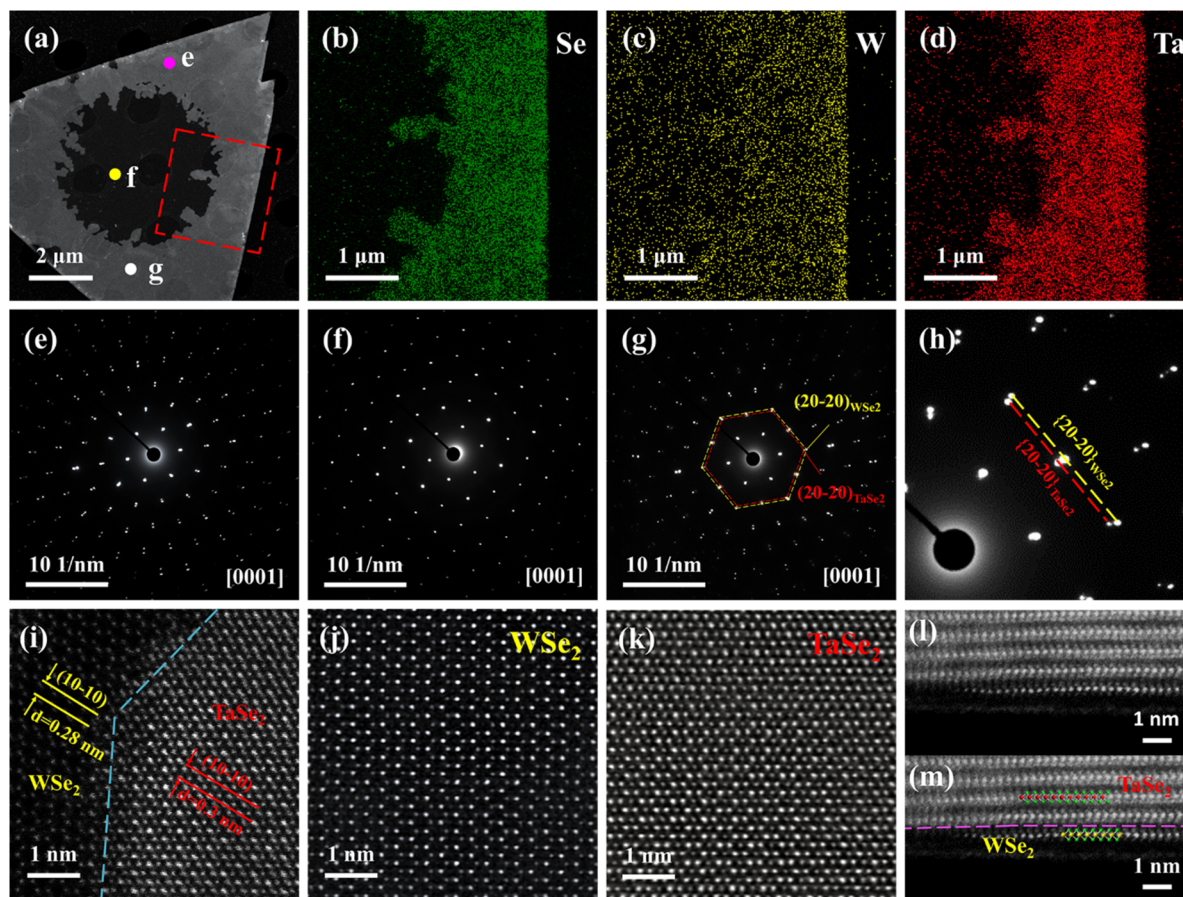
Fig. 2 (a) Low-magnification HAADF-STEM image of the 2D TaSe$_2$-WSe$_2$ heterostructure. The stacked regions are labeled with purple dot e and white dot g, and the underlying single-layer WSe$_2$ is labeled with a yellow dot f. (b–d) EDS elemental maps of the 2D heterostructure (red dashed area) for Se, W, and Ta, respectively. (e–g) SAED patterns from the labeled regions (dots e–g) in (a), respectively. (h) Partially enlarged view of the SAED pattern in (g). (i) High-magnification HAADF-STEM image of the interface between the underlying WSe$_2$ and the stacked TaSe$_2$. (j) and (k) Atomic-resolution HAADF-STEM images of WSe$_2$ and TaSe$_2$. (l) and (m) Atomic-resolution cross-sectional HAADF-STEM images with the corresponding atomic model for multilayer 1T-TaSe$_2$ (upper layer) and monolayer 2H-WSe$_2$ (bottom layer).

layer 2H-WSe$_2$ across the vdWs gap without any atomic intermixing or damage. Additionally, HAADF-STEM analysis of cross-sectional samples of a 2D multilayer TaSe$_2$ and multilayer WSe$_2$ heterostructure (Fig. S7†) shows that the metal–semiconductor contact interface obtained by chemical vapor phase epitaxial growth is very clean and free of defects. Together, all of these TEM studies prove the successful epitaxy of 1T-TaSe$_2$ on 2H-WSe$_2$ without interlayer rotation misfit. According to published references,[45–47] this commensurate TMD heterostructure is expected to reduce the contact resistance compared with that of the randomly twisted stacks, thus showing great application potential in high-performance electronic devices.

To clarify the underlying mechanism for the exceptional performance of the device based on the 2D TaSe$_2$-WSe$_2$ heterostructure, the interfacial energy level alignment was analyzed using a Kelvin probe force microscope (KPFM). The synthesized 2D metal–semiconductor heterostructures were initially transferred to a Si substrate using a PMMA-assisted transfer method. An AFM morphology image of the 2D TaSe$_2$-WSe$_2$ heterostructure on the Si substrate is presented in Fig. 3a, revealing that multilayer metallic TaSe$_2$ is coherently stacked on the edge of the monolayer WSe$_2$ with an edge height of ~19 nm. The local surface potential was determined by detecting the interaction between the conductive AFM probe and the sample. As depicted in Fig. 3b, the multilayer TaSe$_2$ displays weaker contrast than the inner monolayer WSe$_2$, while both exhibit stronger contrast with the Si substrate. The local surface potential (V_{CPD}) is specifically calculated using the following equation:

$$eV_{CPD} = \Phi_{tip} - \Phi_{sample} \quad (1)$$

where e is the charge of an electron. As a result, the Fermi-level difference between WSe$_2$ and TaSe$_2$ can be estimated from the KPFM characterization using the following formula:

$$\Delta E_F = E_F(WSe_2) - E_F(TaSe_2)$$
$$= \Phi_{TaSe_2} - \Phi_{WSe_2} = eV_{CPD}(WSe_2) - eV_{CPD}(TaSe_2) \quad (2)$$

Fig. 3 (a) AFM topography image and height profile of a representative 2D TaSe$_2$-WSe$_2$ heterostructure. (b) KPFM surface potential maps of a transferred 2D TaSe$_2$-WSe$_2$ heterostructure on a conductive Si substrate. (c) Contact potential difference along the red dashed line in (b). (d) Corresponding schematics of the band profiles for the 2D TaSe$_2$-WSe$_2$ heterostructure according to KPFM characterization.

where the Fermi-levels of WSe$_2$ and TaSe$_2$ are denoted by $E_F(WSe_2)$ and $E_F(TaSe_2)$, respectively. Φ_{WSe_2} and Φ_{TaSe_2} are the work functions of WSe$_2$ and TaSe$_2$, respectively. The local surface potentials of WSe$_2$ and TaSe$_2$ are $V_{CPD}(WSe_2)$ and $V_{CPD}(TaSe_2)$, respectively. From the line profile of the surface potential shown in Fig. 3c, the Fermi-level difference between WSe$_2$ and TaSe$_2$ is estimated to be approximately 680 meV using eqn (2). This suggests that TaSe$_2$ possesses a markedly higher work function than WSe$_2$ at the vacuum level. It is worth noting that monolayer WSe$_2$, synthesized *via* CVD, has been widely acknowledged as a p-type semiconductor.[48,49] Upon the intimate contact of TaSe$_2$ and WSe$_2$, electrons will migrate from WSe$_2$ to TaSe$_2$ until equilibrium is reached, resulting in the formation of a depletion region near the heterostructure interface, as depicted in Fig. 3d. Based on the physics of metal–semiconductor junctions, when the work function of the semiconductor is less than that of the metal, an Ohmic-type contact forms at the junction of a metal and a p-type semiconductor.[50]

Given its distinctive metallic properties, 2D TaSe$_2$ is an excellent electrode material for the fabrication of electronic and optoelectronic devices based on 2D materials (Fig. S8†).[51] As shown in Fig. 2l and Fig. S7,† TEM analysis of a cross-sectional sample of 2D TaSe$_2$-WSe$_2$ reveals that the upper multilayer TaSe$_2$ is coherently stacked on a monolayer and multi-layer of WSe$_2$ across the vdWs gap without any atomic intermixing or damage. Consequently, compared to traditional thermal evaporation methods, the two-step CVD approach facilitates the epitaxial growth of electrodes, which effectively circumvents damage to the monolayer WSe$_2$ by high-energy

metal atoms, thereby reducing surface defects and the Fermi-level pinning effect and enhancing contact performance. Furthermore, to study the epitaxial vdWs contact properties of the TaSe$_2$–WSe$_2$ heterostructure, a series of back-gated FETs were fabricated. Fig. S9† schematically illustrates the process of device preparation. Initially, the heterojunction acquired by two-step CVD growth on sapphire was transferred to (n++) 300 nm-SiO$_2$/Si substrates by the PMMA method. Subsequently, the heterostructures were etched in a helium ion microscope (HIM) using a focused helium ion beam to obtain TaSe$_2$–WSe$_2$ heterostructure ribbons. Finally, 5 nm of Cr and 50 nm of Au were deposited as electrodes by standard electron-beam lithography and thermal evaporation. Further details can be found in the Experimental section. The FETs used the TaSe$_2$–WSe$_2$ heterostructure with WSe$_2$ as the channel semiconductor and TaSe$_2$ nanosheets as the source and drain electrode contacts (Cr/Au metal electrodes were deposited on metallic TaSe$_2$ nanosheets). Fig. 4a and the inset of Fig. 4b depict the schematic model and OM of the FET device based on the TaSe$_2$–WSe$_2$ heterostructure, whereas Fig. 4d and the inset of Fig. 4e show a similar Cr/Au-contacted device constructed on WSe$_2$ for comparison. The I_{ds}–V_{ds} output curve with vdWs TaSe$_2$ contacts (Fig. 4b) is much more linear than that with deposited Cr/Au contacts (Fig. 4e), indicating significantly smaller Schottky barriers in the FET device based on the TaSe$_2$–WSe$_2$ heterostructure. Fig. 4c and f display p-type transfer characteristic curves (I_{ds}–V_g) for TaSe$_2$–WSe$_2$ and WSe$_2$ FET devices. The on-state currents of the TaSe$_2$-contacted and Cr/Au-contacted WSe$_2$ devices are 19 and 5.3 µA at $V_d = 0.6$ V. Meanwhile, the TaSe$_2$-contacted FET device has an extraordinary on/off ratio exceeding 10^5 at $V_d = 0.2$ V, which is much larger than that of the Cr/Au-WSe$_2$ FET device (on/off ratio 10^3). The field-effect mobilities for the TaSe$_2$-contacted and Cr/Au-contacted WSe$_2$ FETs are estimated to be 23.5 and 8.7 cm^2 V^{-1} s^{-1} at $V_d = 0.2$ V, respectively. The on-state current and mobility of the obtained TaSe$_2$-contacted WSe$_2$ FETs are much higher than those of the Cr/Au-contacted WSe$_2$ FETs, which indicate that TaSe$_2$ as an *in situ*-grown metal electrode on WSe$_2$ can provide superior electrical properties. In addition, we have prepared WSe$_2$ FET devices with TaSe$_2$ and Cr/Au contacts on the same heterostructure and obtained similar experimental results with higher performance for TaSe$_2$ contacts (Fig. S10†). It is essential to obtain the Schottky barrier height (Φ_{SB}) to better understand the charge transport feature in the WSe$_2$ device. Experiments with temperature variations were performed to further explore the Φ_{SB} value of the device. The Φ_{SB} value is then extracted under flat-band conditions. According to Fig. S11e and f,† Φ_{SB} values are around 151 meV (Cr/Au-contacted FET) and 52 meV (TaSe$_2$-contacted FET), respectively. This shows that epitaxial growth of TaSe$_2$ can effectively reduce the Schottky barrier for WSe$_2$ devices. These results demonstrate that the epitaxial growth of 2D TaSe$_2$-WSe$_2$ by a two-step CVD method greatly improves the contact between metal and 2D semiconductors. This work is an important step forward in expanding the range of novel heterostructure materials that can provide more potential applications for high-performance electronic devices.

(a) ... **(b)** ... **(c)**

(d) ... **(e)** ... **(f)**

Fig. 4 (a) 3D schematic model of the FET device based on the 2D $TaSe_2$-WSe_2 heterostructure. (b) Characteristic I_{ds}–V_{ds} output curves of the 2D $TaSe_2$-WSe_2 heterostructure at different back-gate voltages. Inset shows an optical image of the 2D $TaSe_2$-WSe_2 FET device. (c) Characteristic transfer curves (I_{ds} – V_g) of the 2D $TaSe_2$-WSe_2 heterostructure. (d) 3D schematic model of the FET device based on the as-grown WSe_2 on the 300 nm-SiO_2/Si substrate. (e) I_{ds}–V_{ds} output curves of the WSe_2 device collected at room temperature. Inset shows an optical image of a two-electrode WSe_2 device. (f) Characteristic transfer curves of the WSe_2 device.

Conclusions

In summary, 2D layered $TaSe_2$-WSe_2 metal–semiconductor heterostructures have been synthesized on sapphire substrates by depositing $TaSe_2$ on pre-synthesized 2H-WSe_2 monolayers using a simple two-step CVD method. TEM studies reveal a clean interface and vdWs epitaxial relationship for $(20{-}20)_{TaSe_2}$//$(20{-}20)_{WSe_2}$ and $[0001]_{TaSe_2}$//$[0001]_{WSe_2}$ in 2D $TaSe_2$-WSe_2 heterostructures. Furthermore, the analysis of surface potential and electrical transport measurements of this 2D heterostructure reveals that the heterojunction has higher field-effect mobility and on/off ratio. The enhancement of the electronic behavior by the epitaxial growth of metallic vdWs-layered materials can expand the range of metal–semiconductor vertical heterostructure materials and improve the performance of 2D electronic devices.

Conflicts of interest

There are no conflicts to declare.

Acknowledgements

References

1 G. E. Moore, *Proc. IEEE*, 1998, **86**, 82–85.
2 M. Lundstrom, *Science*, 2003, **299**, 210–211.
3 X. Zhang, Z. C. Lai, Q. L. Ma and H. Zhang, *Chem. Soc. Rev.*, 2018, **47**, 3301–3338.
4 J. P. Shi, M. Hong, Z. P. Zhang, Q. Q. Ji and Y. F. Zhang, *Coord. Chem. Rev.*, 2018, **376**, 1–19.
5 J. Zhou, J. Lin, X. Huang, Y. Zhou, Y. Chen, J. Xia, H. Wang, Y. Xie, H. Yu, J. Lei, D. Wu, F. Liu, Q. Fu, Q. Zeng, C.-H. Hsu, C. Yang, L. Lu, T. Yu, Z. Shen, H. Lin, B. I. Yakobson, Q. Liu, K. Suenaga, G. Liu and Z. Liu, *Nature*, 2018, **556**, 355–359.
6 M. Chhowalla, H. S. Shin, G. Eda, L. J. Li, K. P. Loh and H. Zhang, *Nat. Chem.*, 2013, **5**, 263–275.
7 M. Chhowalla, D. Jena and H. Zhang, *Nat. Rev. Mater.*, 2016, **1**, 16052.
8 J. Xia, X. Huang, L. Z. Liu, M. Wang, L. Wang, B. Huang, D. D. Zhu, J. J. Li, C. Z. Gu and X. M. Meng, *Nanoscale*, 2014, **6**, 8949–8955.
9 J. Xia, Y. X. Zhao, L. Wang, X. Z. Li, Y. Y. Gu, H. Q. Cheng and X. M. Meng, *Nanoscale*, 2017, **9**, 13786–13793.
10 H. N. Jaiswal, M. Liu, S. Shahi, S. Wei, J. Lee, A. Chakravarty, Y. Guo, R. Wang, J. M. Lee, C. Chang, Y. Fu,

R. Dixit, X. Liu, C. Yang, F. Yao and H. Li, *Adv. Mater.*, 2020, **32**, 2002716.

11 L. Song, L. Ci, H. Lu, P. B. Sorokin, C. Jin, J. Ni, A. G. Kvashnin, D. G. Kvashnin, J. Lou, B. I. Yakobson and P. M. Ajayan, *Nano Lett.*, 2010, **10**, 3209–3215.

12 K. F. Mak, C. Lee, J. Hone, J. Shan and T. F. Heinz, *Phys. Rev. Lett.*, 2010, **105**, 136805.

13 J.-G. Song, J. Park, W. Lee, T. Choi, H. Jung, C. W. Lee, S.-H. Hwang, J. M. Myoung, J.-H. Jung, S.-H. Kim, C. Lansalot-Matras and H. Kim, *ACS Nano*, 2013, **7**, 11333–11340.

14 D. Wolverson, S. Crampin, A. S. Kazemi, A. Ilie and S. J. Bending, *ACS Nano*, 2014, **8**, 11154–11164.

15 M. Chhowalla, H. S. Shin, G. Eda, L.-J. Li, K. P. Loh and H. Zhang, *Nat. Chem.*, 2013, **5**, 263–275.

16 Y. M. Shi, H. N. Li and L. J. Li, *Chem. Soc. Rev.*, 2015, **44**, 2744–2756.

17 P. Wang, Y. Huan, P. Yang, M. Cheng, J. Shi and Y. Zhang, *Acc. Mater. Res.*, 2021, **2**, 751–763.

18 Z. Zhang, P. Yang, M. Hong, S. Jiang, G. Zhao, J. Shi, Q. Xie and Y. Zhang, *Nanotechnology*, 2019, **30**, 182002.

19 L. Xie, M. Liao, S. Wang, H. Yu, L. Du, J. Tang, J. Zhao, J. Zhang, P. Chen, X. Lu, G. Wang, G. Xie, R. Yang, D. Shi and G. Zhang, *Adv. Mater.*, 2017, **29**, 1702522.

20 S. B. Desai, S. R. Madhvapathy, A. B. Sachid, J. P. Llinas, Q. X. Wang, G. H. Ahn, G. Pitner, M. J. Kim, J. Bokor, C. M. Hu, H. S. P. Wong and A. Javey, *Science*, 2016, **354**, 99–102.

21 F. Wu, H. Tian, Y. Shen, Z. Hou, J. Ren, G. Gou, Y. Sun, Y. Yang and T.-L. Ren, *Nature*, 2022, **603**, 259–264.

22 A. Allain, J. Kang, K. Banerjee and A. Kis, *Nat. Mater.*, 2015, **14**, 1195–1205.

23 J. Tan, S. Li, B. Liu and H. M. Cheng, *Small Struct.*, 2021, **2**, 2000093.

24 A. Razavieh, P. Zeitzoff and E. J. Nowak, *IEEE Trans. Nanotechnol.*, 2019, **18**, 999–1004.

25 S. G. Louie and M. L. Cohen, *Phys. Rev. B: Solid State*, 1976, **13**, 2461–2469.

26 C. Kim, I. Moon, D. Lee, M. S. Choi, F. Ahmed, S. Nam, Y. Cho, H.-J. Shin, S. Park and W. J. Yoo, *ACS Nano*, 2017, **11**, 1588–1596.

27 T. Nishimura, K. Kita and A. Toriumi, *Appl. Phys. Lett.*, 2007, **91**, 123123.123121–123123.123123.

28 A. Pirkle, J. Chan, A. Venugopal, D. Hinojos, C. W. Magnuson, S. McDonnell, L. Colombo, E. M. Vogel, R. S. Ruoff and R. M. Wallace, *Appl. Phys. Lett.*, 2011, **99**, 122108–122108.

29 J. Jang, H.-S. Ra, J. Ahn, T. W. Kim, S. H. Song, S. Park, T. Taniguch, K. Watanabe, K. Lee and D. K. Hwang, *Adv. Mater.*, 2022, **34**, 2109899.

30 Z. H. Cheng, Y. F. Yu, S. Singh, K. Price, S. G. Noyce, Y. C. Lin, L. Y. Cao and A. D. Franklin, *Nano Lett.*, 2019, **19**, 5077–5085.

31 A. Jain, A. Szabo, M. Parzefall, E. Bonvin, T. Taniguchi, K. Watanabe, P. Bharadwaj, M. Luisier and L. Novotny, *Nano Lett.*, 2019, **19**, 6914–6923.

32 R. Kappera, D. Voiry, S. E. Yalcin, B. Branch, G. Gupta, A. D. Mohite and M. Chhowalla, *Nat. Mater.*, 2014, **13**, 1128.

33 J. H. Sung, H. Heo, S. Si, Y. H. Kim, H. R. Noh, K. Song, J. Kim, C. S. Lee, S. Y. Seo, D. H. Kim, H. K. Kim, H. W. Yeom, T. H. Kim, S. Y. Choi, J. S. Kim and M. H. Jo, *Nat. Nanotechnol.*, 2017, **12**, 1064–1070.

34 X. Cui, G. H. Lee, Y. D. Kim, G. Arefe, P. Y. Huang, C. H. Lee, D. A. Chenet, X. Zhang, L. Wang, F. Ye, F. Pizzocchero, B. S. Jessen, K. Watanabe, T. Taniguchi, D. A. Muller, T. Low, P. Kim and J. Hone, *Nat. Nanotechnol.*, 2015, **10**, 534–540.

35 Y. Liu, J. Guo, E. Zhu, L. Liao, S.-J. Lee, M. Ding, I. Shakir, V. Gambin, Y. Huang and X. Duan, *Nature*, 2018, **557**, 696–700.

36 X. K. Zhai, X. Xu, J. B. Peng, F. L. Jing, Q. L. Zhang, H. J. Liu and Z. G. Hu, *ACS Appl. Mater. Interfaces*, 2020, **12**, 24093–24101.

37 Z. P. Zhang, Y. Gong, X. L. Zou, P. Liu, P. F. Yang, J. P. Shi, L. Y. Zhao, Q. Zhang, L. Gu and Y. F. Zhang, *ACS Nano*, 2019, **13**, 885–893.

38 Y. Zhang, L. Yin, J. W. Chu, T. A. Shifa, J. Xia, F. Wang, Y. Wen, X. Y. Zhan, Z. X. Wang and J. He, *Adv. Mater.*, 2018, **30**, 1803665.

39 Q. D. Fu, X. W. Wang, J. D. Zhou, J. Xia, Q. S. Zeng, D. H. Lv, C. Zhu, X. L. Wang, Y. Shen, X. M. Li, Y. N. Hua, F. C. Liu, Z. X. Shen, C. H. Jin and Z. Liu, *Chem. Mater.*, 2018, **30**, 4001–4007.

40 C. S. Lee, S. J. Oh, H. Heo, S. Y. Seo, J. Kim, Y. H. Kim, D. Kim, O. F. N. Okello, H. Shin, J. H. Sung, S. Y. Choi, J. S. Kim, J. K. Kim and M. H. Jo, *Nano Lett.*, 2019, **19**, 1814–1820.

41 V. T. Vu, T. T. H. Vu, T. L. Phan, W. T. Kang, Y. R. Kim, M. D. Tran, H. T. T. Nguyen, Y. H. Lee and W. J. Yu, *ACS Nano*, 2021, **15**, 13031–13040.

42 P. Y. Qiao, J. Xia, X. Z. Li, F. Ru, P. Liu, L. F. Tian, X. X. Jiang, Z. S. Lin, X. Chen and X. M. Meng, *Adv. Funct. Mater.*, 2022, **32**, 2201449.

43 B. L. Liu, M. Fathi, L. Chen, A. Abbas, Y. Q. Ma and C. W. Zhou, *ACS Nano*, 2015, **9**, 6119–6127.

44 J. C. Tsang, J. E. Smith, M. W. Shafer and S. F. Meyer, *Phys. Rev. B: Solid State*, 1977, **16**, 4239–4245.

45 J. Zhang, J. H. Wang, P. Chen, Y. Sun, S. Wu, Z. Y. Jia, X. B. Lu, H. Yu, W. Chen, J. Q. Zhu, G. B. Xie, R. Yang, D. X. Shi, X. L. Xu, J. Y. Xiang, K. H. Liu and G. Y. Zhang, *Adv. Mater.*, 2016, **28**, 1950–1956.

46 M. Liao, Z.-W. Wu, L. Du, T. Zhang, Z. Wei, J. Zhu, H. Yu, J. Tang, L. Gu, Y. Xing, R. Yang, D. Shi, Y. Yao and G. Zhang, *Nat. Commun.*, 2018, **9**, 4068.

47 K. Liu, L. Zhang, T. Cao, C. Jin, D. Qiu, Q. Zhou, A. Zettl, P. Yang, S. G. Louie and F. Wang, *Nat. Commun.*, 2014, **5**, 4966.

48 Y. Gao, Y. L. Hong, L. C. Yin, Z. T. Wu, Z. Q. Yang, M. L. Chen, Z. B. Liu, T. Ma, D. M. Sun, Z. H. Ni, X. L. Ma, H. M. Cheng and W. C. Ren, *Adv. Mater.*, 2017, **29**, 1700990.

49 Q. Cheng, J. Pang, D. Sun, J. Wang, S. Zhang, F. Liu, Y. Chen, R. Yang, N. Liang, X. Lu, Y. Ji, J. Wang,

C. Zhang, Y. Sang, H. Liu and W. Zhou, *InfoMat*, 2020, **2**, 656–697.

50 S. M. Sze and K. K. Ng, *Physics of semiconductor devices*, Wiley-Interscience, Hoboken, N.J., 3rd edn, 2007.

51 J. Shi, X. Chen, L. Zhao, Y. Gong, M. Hong, Y. Huan, Z. Zhang, P. Yang, Y. Li, Q. Zhang, Q. Zhang, L. Gu, H. Chen, J. Wang, S. Deng, N. Xu and Y. Zhang, *Adv. Mater.*, 2018, **30**, 1804616.